



# Influence of Isothermal Holding on the Microstructure and Mechanical Properties of Electron Beam Welded Dissimilar Inconel 718/ATI 718Plus<sup>®</sup> Joint

Oskar Dziuba, Grzegorz Cempura, Agnieszka Wusatowska-Sarnek, and Adam Kruk

(Submitted September 1, 2019; in revised form December 13, 2019; published online January 23, 2020)

**Microstructural changes of the Inconel 718 and ATI 718Plus<sup>®</sup> base materials and the fusion zone caused by the isothermal hold at 760 °C for up to 500 h were investigated. The evaluation was performed using a scanning electron microscope with backscattered electrons detector and scanning transmission electron microscopy supported by energy-dispersive x-ray spectroscopy. Furthermore, to evaluate the effect of microstructural changes on mechanical properties Vickers microhardness measurements were performed. Exposure of welded joint at high temperature led to coarsening and/or dissolution of main strengthening phases' particles and nucleation and growth of plate-like precipitates. In the interdendritic region of the fusion zone, the transformation of the Laves phase to a complex cluster of precipitates contained  $\sigma$  phase had taken place. Analysis of microstructure and microhardness measurements showed that ATI 718Plus has better mechanical properties and microstructural stability at elevated temperature than Inconel 718.**

**Keywords** superalloys, electron beam welding, ATI 718Plus, Inconel 718, electron microscopy, FIB-SEM tomography

## 1. Introduction

Inconel 718 (IN718) is the most popular precipitation-strengthened nickel-based superalloy introduced by the Huntington Alloys Division of INCO in 1959 (Ref 1). The IN718 is strengthened mainly by body-centered tetragonal  $\gamma''$ -Ni<sub>3</sub>(Al, Ti, Nb) phase and face-centered cubic  $\gamma'$ -Ni<sub>3</sub>(Al, Ti) phase. Its remarkable properties, including high strength, corrosion resistance, excellent creep resistance and good toughness up to about 650 °C, enabled the broad application of IN718 in aircraft and land-based gas turbine engines and components for liquid-fueled rockets (Ref 2, 3).

ATI 718Plus<sup>®</sup> (718Plus) is a precipitation-strengthened nickel-based superalloy which has been developed by ATI Allvac company at the beginning of the twenty-first century. The 718Plus is the first Ni-based superalloy intended for both rotating and static parts which may be used in power generation

industry, aviation and aerospace industry (Ref 4, 5). The chemical composition of this alloy is a modification of IN718. The principal difference in 718Plus chemistry is lower Ti-to-Al ratio as well as lower amount of Fe, which is replaced by the addition of Co and W. These modifications led to replacement of metastable  $\gamma''$  main strengthening phase in IN718 with more stable  $\gamma'$  phase in 718Plus that caused a increase in thermal stability up to 704 °C. Other constituents of 718Plus microstructure are  $\gamma$  matrix and precipitates of hexagonal  $\eta$ -Ni<sub>3</sub>Ti,  $\eta^*$ -Ni<sub>6</sub>AlNb or Ni<sub>6</sub>(Al, Ti)Nb phases distributed mainly at the grain boundaries (Ref 6-9).

Welding is one of the most critical processes used during both manufacturing and repairing components made of the alloys in question for the above-mentioned industries (Ref 10). The high temperature that occurs during welding process may cause microstructural changes, including alteration of both size and volume fraction of strengthening phases that may lead to a decrease in mechanical properties in the fusion zone (FZ) and heat-affected zones. Both IN718 and 718Plus are described as well weldable alloys, but under certain conditions they are susceptible to heat-affected zone liquation cracking and Nb segregation to interdendritic regions of FZ leading to precipitation of brittle Laves phase (Ref 11-13).

Electron beam welding (EBW) is one of the most important joining processes for precipitation-strengthened Ni-based superalloys including IN718 and 718Plus because of the advantages of this process such as low level of distortions and narrow heat-affected zone. On the other hand, the main disadvantages of EBW process are expensive equipment and the necessity of conducting the process in vacuum (Ref 14, 15).

## 2. Experimental Materials and Methods

The IN718 and 718Plus superalloys used in this study were commercially produced by vacuum induction melting and vacuum arc remelting followed by rotary forging and ring

This article is an invited submission to JMEPEG selected from presentations at The XXII Physical Metallurgy and Materials Science Conference: Advanced Materials and Technologies (AMT 2019) held June 9-12, 2019, in Bukowina Tatrzańska, Poland, and has been expanded from the original presentation.

Oskar Dziuba, Grzegorz Cempura, and Adam Kruk, International Centre of Electron Microscopy for Materials Science and Faculty of Metals Engineering and Industrial Computer Science, AGH University of Science and Technology (AGH-UST), al. Mickiewicza 30, 30-059 Kraków, Poland; and Agnieszka Wusatowska-Sarnek, Pratt & Whitney, 400 Main Street, East Hartford, CT 06108. Contact e-mail: odziuba@agh.edu.pl.

**Table 1** Nominal chemical compositions of 718Plus and IN718, wt.%

| Element | Ni   | Cr   | Fe   | Co  | Nb + Ta | Mo  | Al  | Ti   | W   | C    |
|---------|------|------|------|-----|---------|-----|-----|------|-----|------|
| 718Plus | Bal. | 18.0 | 9.7  | 9.2 | 5.5     | 2.7 | 1.5 | 0.75 | 1.0 | 0.02 |
| IN718   | Bal. | 18.1 | 19.0 | ... | 5.3     | 3.0 | 0.7 | 0.9  | ... | 0.03 |

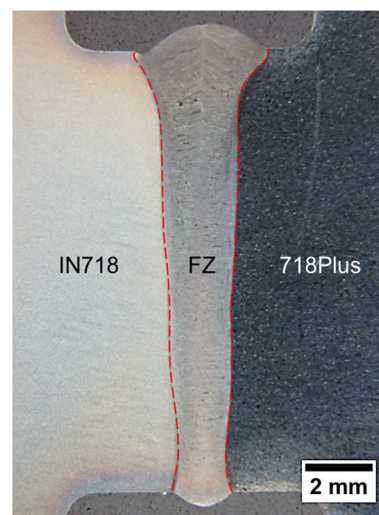
rolling. The as-received material had undergone a standard heat treatment that consisted of solution treatment and two-step aging. The chemical compositions of the investigated alloys are shown in Table 1. The IN718 and 718Plus rings were autogenously welded with electron beam using industrial equipment. In order to perform isothermal hold followed by metallographic investigations and microhardness measurements, the dissimilar joint was sectioned transversely to the welding direction using a manual cut-off machine Struers Labotom 5. These samples were isothermally held at 760 °C for 10, 25, 50, 100 and 500 h and then air-cooled. The cross-sectional samples were hot-mounted in conductive resin, followed by grinding with SiC papers up to the grit size of 4000. Three-step polishing consisted of 3- $\mu$ m diamond suspension polishing, following by aluminum oxide and silica oxide suspensions final polishing. Chemical etching using Kalling's reagent was used to reveal the structure of the investigated joint for optical macrography purposes.

The optical macrograph of the investigated joint was taken using Zeiss SteREO Discovery.V12 stereo microscope. The base materials and the FZ microstructures were investigated using field emission Zeiss Merlin Gemini II scanning electron microscope (SEM) equipped with Quantax 800 energy-dispersive x-ray spectroscopy (EDX) microanalysis system. The STEM-EDX analysis and HRSTEM investigations of an interdendritic region of the FZ that was isothermally held for 500 h were performed on the lamella cut out from the middle area of the fusion zone's axis by FIB-SEM Zeiss Neon CrossBeam 40EsB using FEI Titan Cubed G2 60-300 with ChemiSTEM™ system. Phases present in the investigated joint were identified by means of selected area electron diffraction (SAED) supported by JEMS software.

The microstructures of both base materials and the FZ were analyzed by quantitative image analysis. The SEM-BSE images of the above-mentioned regions were binarized in order to distinguish the  $\gamma$  matrix and precipitates of phases present in examined samples. The volume fractions of precipitates were calculated as the sum of areas of all particles divided by the total area of the image.

3D imaging of microstructure of both base materials and FZ was performed using FIB-SEM tomography. The Zeiss Neon CrossBeam 40EsB with Ga<sup>+</sup> ion beam at parameters: 30 kV, 200 pA and a aperture of 60  $\mu$ m was used to perform in situ milling with an approximately 8 nm step. The SEM images of milled area were recorded at 1.7 kV accelerating voltage with a voxel size of 8 nm  $\times$  8 nm  $\times$  8 nm using backscattered electrons detector. From the series of obtained SEM-BSE images, the 3D reconstruction of the investigated areas of welded joint was generated using Avizo Fire 6.3 software.

To evaluate the effects of welding thermal cycle and isothermal hold up to 500 h on mechanical properties of the welded joint, microhardness measurements were taken using Wilson-Hardness Tukon 2500 Vickers hardness tester with a load of 4.90 N (HV0.5) for 10 s.

**Fig. 1** Cross-sectional macrograph of the EBW joint

### 3. Results

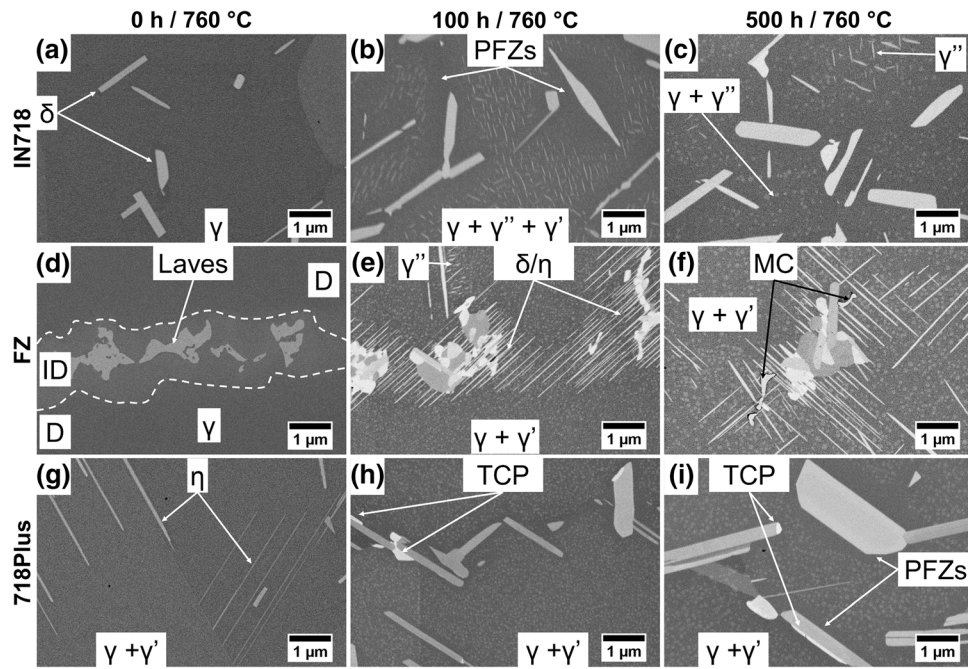
The optical macrograph showing the cross section of the EBW joint is shown in Fig. 1. The needle-like shape fusion zone is narrow, and the HAZs are not visible at such magnification. Insubstantial undercut on the IN718 base material side was observed.

#### 3.1 SEM-BSE Analysis and FIB-SEM Tomography

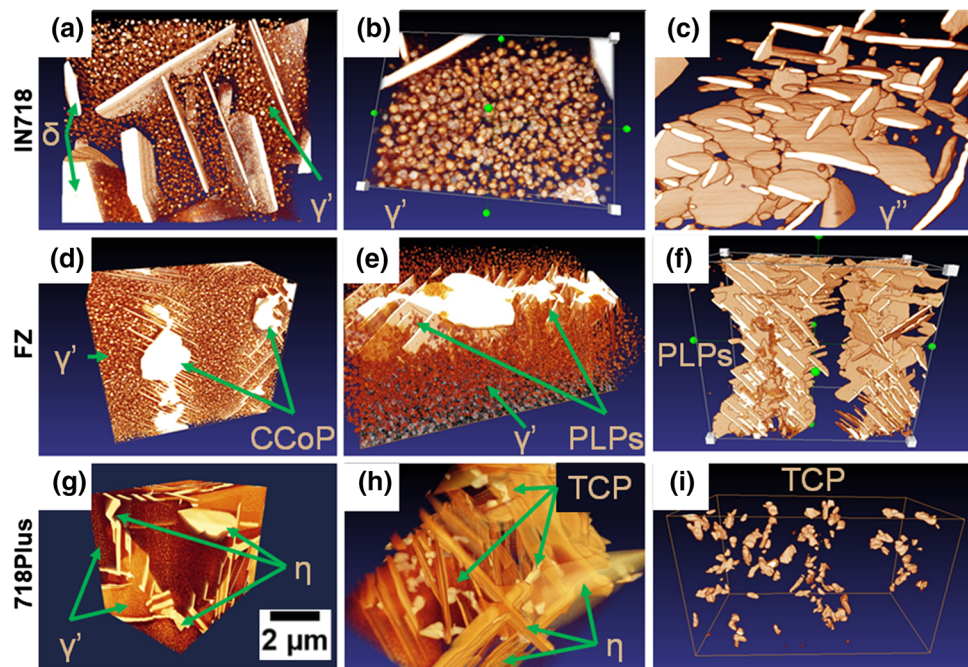
Figure 2(a)-(c) shows SEM-BSE images of the IN718 base material in as-welded state and after heat treatment for 100 and 500 h. It is clearly seen that both the volume fraction of plate-like precipitates and the size of the main strengthening phases ( $\gamma''$  and  $\gamma'$ ) increase with increasing time. Moreover, after 500 h of isothermal hold the  $\gamma''$  precipitates are hardly visible. Quantitative analysis of this region shows an increase in volume fraction of plate-like precipitates from about 3.6% in as-welded condition up to about 13.5% after 500 h of post-weld heat treatment.

Figure 2(d)-(f) presents SEM-BSE images of FZ in as-welded state and after heat treatment for 100 and 500 h. In this area, the coarsening of main strengthening phases along both dendrites and interdendritic regions can be observed. In particular, it can be seen that after post-weld heat treatment there are differences between brightness of precipitates along the interdendritic regions which suggest differences in their chemical composition. Furthermore, it is clearly seen that the volume fraction of plate-like precipitates along interdendritic regions increases with increasing time of isothermal hold (about 1.9% before and about 14.3% after 500 h).

SEM-BSE images of 718Plus base material in as-welded condition and after isothermal hold for 100 and 500 h are



**Fig. 2** SEM-BSE images of IN718 (a-c), fusion zone (d-f) and 718Plus (g-i) in as-welded condition (a, d, g), after 100 h of isothermal hold (b, e, h) and after 500 h of isothermal hold (c, f, i) (D-dendrites, ID-interdendritic regions)



**Fig. 3** 3D visualization of selected areas of base materials and fusion zone after isothermal hold at 760 °C for 500 h: (a-c) IN718 base material, (d-f) fusion zone, (g-i) 718Plus base material; (CCoP-complex clusters of precipitates, PLPs-plate-like precipitates)

shown in Fig. 2(g)-(i). In contrary to the IN718, the increase in volume fraction of plate-like precipitates is less pronounced (only up to about 6.6%). The spheroidal  $\gamma'$  precipitates are

visibly coarser after 500 h of isothermal hold. It can be seen that after post-weld heat treatment some brighter precipitates are present near the plate-like precipitates.



It can be seen in Fig. 2(a)-(c) and (g)-(i) that in the parent materials of IN718 and 718Plus denuded zones form around larger precipitates of both  $\delta$  and  $\eta$  phases.

Three-dimensional visualizations of FIB-SEM reconstructed volumes of IN718, the FZ and 718Plus are shown in Fig. 3(a)-(i). Figure 3(b) and (c) presents spatial distribution of spheroidal  $\gamma'$  phase and coarsen detritus of  $\gamma''$  phase precipitates in the heat-treated IN718 base material, respectively. In Fig. 3(e) and (f), a more detailed analysis of the tomographic reconstruction of precipitates present in heat-treated FZ is presented. It can be seen that in this area plate-like precipitates of  $\eta/\delta$  grow on the surface of the complex cluster of precipitates localized in the core of interdendritic regions. Figure 3(h) presents that TCP phase precipitates nucleates heterogeneously on the surfaces of plate-like precipitates. The spatial distribution of TCP phases' precipitates in the analyzed volume of heat-treated 718Plus is shown in Fig. 3(i).

### 3.2 STEM-EDX and SAED Analysis

Figure 4(a)-(j) shows a scanning transmission electron microscopy high-angle annular dark field (STEM-HAADF) image of the microstructure (Fig. 4a) and EDX maps of selected chemical elements (Fig. 4b-j) of the interdendritic region of the near fusion zone's axis area heat-treated for 500 h. The average chemical composition of phases present in the interdendritic region determined using STEM-EDX method is shown in Table 2. There are two types of plate-like precipitates. The  $\eta$  phase precipitates are enriched with Ni, Al, Nb and Ti, whereas the precipitates of  $\delta$  phase are enriched only with Ni and Nb. In the center and at the bottom of the analyzed area, there are precipitates enriched with Mo and Cr. The TEM-DF image of the above-mentioned area is shown in Fig. 5(a). SAED analysis (Fig. 5b) of Mo- and Cr-enriched precipitate indicates that is  $\sigma$  phase. Results of HRSTEM-HAADF imaging and theoretical HAADF image of  $\sigma$  phase particle are presented in Fig. 5(c) and (d), respectively. The presence of other phases was confirmed using diffraction examination (TEM-SAED), and these results were reported in our previous study (Ref 16). Nb- and Ti- enriched MC-type carbides can be observed in the core of interdendritic region of FZ (Fig. 5e, i, j). Fine, spheroidal  $\gamma'$  precipitates present in the FZ are enriched with Ni, Nb, Al and Ti (Fig. 5b, e, g, i).

### 3.3 Microhardness Measurements

The changes of microhardness of the welded joint with heat treatment time are presented in Fig. 6. The microhardness of IN718 base material dropped from about 480 HV0.5 in as-welded condition to about 342 HV0.5 after 500 h of isothermal hold, whereas the microhardness of 718Plus base material fell from about 500 HV0.5 to about 436 HV0.5. The hardness of FZ in as-welded condition was roughly 300 HV0.5, but after 10 h of isothermal hold the hardness increased up to about 500 HV0.5. With continued exposure to an elevated temperature, the FZ microhardness decreased to about 434 HV0.5 after 500 h.

## 4. Discussion

The SEM-BSE investigations (Fig. 2a-c) and quantitative analysis of the microstructure of IN718 base material showed two major microstructural changes after heat treatment at

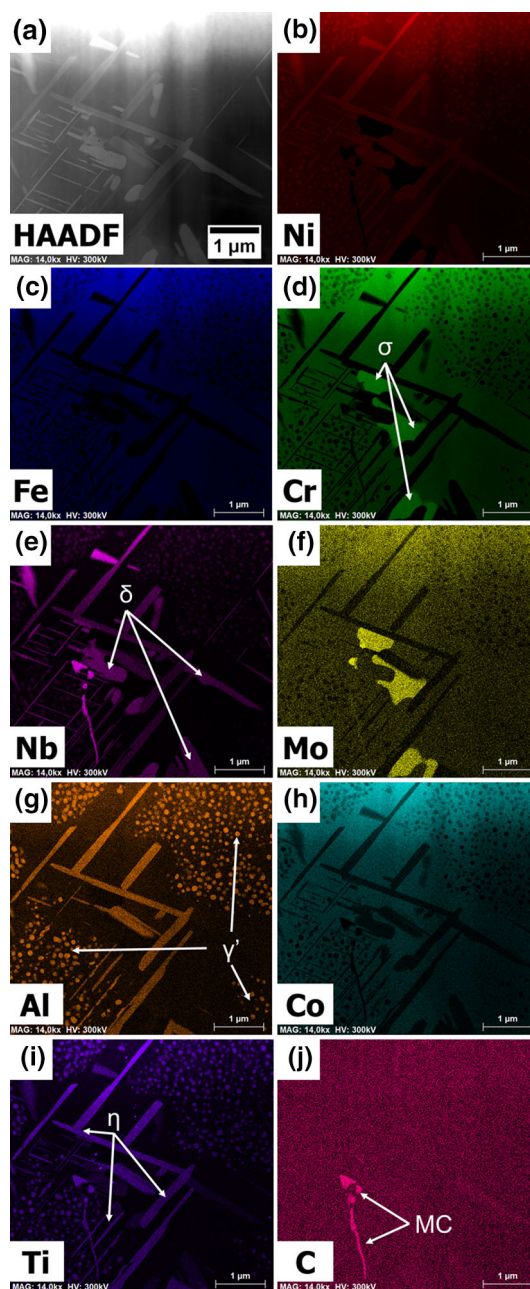


**Fig. 4** (a) STEM-HAADF image of a microstructure of the fusion zone interdendritic region after 500-hrs isothermal hold, (b)-(j) STEM-EDX maps of selected elements

760 °C: formation and growth of  $\delta$  phase particles, and coarsening followed by dissolution of main strengthening phases particles ( $\gamma''$  and  $\gamma'$ ). This observation is in agreement with studies performed by Radavich and Guédou et al. (Ref 17, 18).

The microstructure of as-welded FZ is composed of dendrites and interdendritic regions that exhibit different contrast in SEM-BSE (Fig. 2d). It may suggest that segregation of chemical elements occurred during the solidification of welded material. The above-mentioned phenomena led to formation of both MC-type carbides and Laves phase in the interdendritic regions during the solidification in the FZ (Ref

**Table 2** The average chemical composition of different precipitates developed in the fusion zone after 500 h of isothermal hold

| Analyzed phase | Average chemical composition and standard deviation, at.% |      |      |      |      |      |      |      |      |
|----------------|---|------|------|------|------|------|------|------|------|
|                | Ni  | Cr   | Fe   | Co   | Nb   | Mo   | Al   | Ti   | W    |
| $\gamma$       | 46.8  | 23.6 | 16.7 | 7.0  | 1.0  | 1.9  | 2.4  | 0.3  | 0.3  |
|                | 0.33  | 0.48 | 0.20 | 0.03 | 0.07 | 0.03 | 0.27 | 0.02 | 0.05 |
| $\eta$         | 65.6  | 0.8  | 2.1  | 3.6  | 11.1 | 0.8  | 11.8 | 3.9  | 0.2  |
|                | 0.20  | 0.05 | 0.09 | 0.07 | 0.10 | 0.06 | 0.36 | 0.11 | 0.03 |
| $\delta$       | 66.7  | 1.1  | 1.7  | 4.1  | 19.6 | 2.1  | 2.5  | 1.8  | 0.4  |
|                | 0.29  | 0.09 | 0.24 | 0.17 | 0.41 | 0.35 | 0.31 | 0.29 | 0.10 |
| $\gamma'$      | 65.5  | 1.0  | 2.2  | 2.1  | 6.9  | 0.4  | 18.0 | 3.9  | 0.2  |
|                | 1.25  | 0.21 | 0.35 | 0.07 | 0.60 | 0.22 | 0.73 | 0.47 | 0.05 |
| $\sigma$       | 18.4  | 46.4 | 12.9 | 7.8  | 0.5  | 11.1 | 2.0  | 0.2  | 0.9  |
|                | 0.14  | 0.16 | 0.12 | 0.13 | 0.05 | 0.15 | 0.37 | 0.01 | 0.05 |
| MC             | 2.5   | 2.2  | 0.7  | 0.5  | 77.4 | 3.5  | 1.8  | 11.4 | ...  |
|                | 0.33  | 0.18 | 0.14 | 0.18 | 1.31 | 0.03 | 0.03 | 0.11 |      |

10). Further heat treatment at 760 °C caused a number of microstructural changes in FZ as shown in Fig. 2(d)–(f). Firstly, a transformation of Laves phase into a complex cluster of precipitates was observed, within which sigma phase was identified. Secondly, nucleation and growth of  $\eta/\delta$  plate-like precipitates in the entire cluster was observed. Lastly, post-weld heat treatment caused coarsening of both  $\gamma''$  (within interdendritic regions) and  $\gamma'$  precipitates (within both dendrites and interdendritic regions) and dissolution of  $\gamma''$  precipitates in the interdendritic regions of FZ. Higher thermal stability of  $\gamma'$  phase may be implicitly concluded. To the knowledge of the authors, such observations are documented for the first time.

In contrary to the microstructural changes that occurred in IN718, the base material of 718Plus exhibits higher thermal stability of phases (Fig. 2g–j). After post-weld heat treatment, the increase in plate-like precipitates volume fraction was much lower in 718Plus than in the IN718. Moreover, the coarsening of  $\gamma'$  phase precipitates in 718Plus was not as significant as in other regions of the welded joint. This study is in good agreement with the work of Cao (Ref 9). The brighter (due to BSE contrast mechanism) precipitates observed near the  $\eta$  phase after thermal exposure for 100 and 500 h (Fig. 2h and i) are most likely TCP phases as similar observations made by Krakow et al. (Ref 19).

FIB-SEM tomography of heat-treated welded joint (Fig. 3a–i) revealed the three-dimensional morphology of phases present in investigated areas of the welded joint. The spheroidal precipitates of  $\gamma'$  precipitates were observed in all above-mentioned areas (Fig. 3a, b, d, e, g). The elongated-disk shape  $\gamma''$  particles were visible only in small areas of IN718 (Fig. 3c), whereas they were not observed along interdendritic regions of FZ. It may suggest lower thermal stability of  $\gamma''$ . The 3D images of FZ (Fig. 3d–f) presented that plate-like precipitates in interdendritic regions nucleate and grow in definite orientation relationship with  $\gamma$  matrix. The studies of Pickering et al. indicate Blackburn relationship (Ref 20). 3D visualization of heat-treated 718Plus microstructure (Fig. 3g–i) showed the heterogeneous nucleation of TCP phases on the  $\eta$  plate-like precipitates.

STEM-EDX and HRSTEM investigations (Fig. 4b–j, 5a–d and Table 2) showed that long-term thermal exposure increases the amount of phases present in the interdendritic area from 2 to 5. During the isothermal hold at 760 °C, the reprecipitation of both  $\gamma'$  and  $\gamma''$  occurs. Additionally, the formation and growth of plate-like precipitates was observed as well as Laves to  $\sigma$  phase transformation.

Microstructural changes affected mechanical properties (measured by microhardness) in all investigated areas. The highest loss of microhardness by roughly 28% was observed in IN718 base material, and it was caused mainly by coarsening and/or dissolving of strengthening  $\gamma''$  and  $\gamma'$  phases. On the other hand, microhardness in 718Plus base material did decreased only by roughly 13%. IN718 exhibits lower thermal stability as compared to 718Plus. The hardness of the FZ in as-welded condition was roughly 300 HV0.5. Such low hardness was caused by the lack of  $\gamma'$  and  $\gamma''$  precipitates in the microstructure after solidification with high cooling rate after EBW process. Post-weld heat treatment led to a sizeable increase in microhardness up to approximately 500 HV0.5 in short time of 10 h. It was caused by reprecipitation of  $\gamma'$  and  $\gamma''$  phases. Hold at temperature for longer times yielded in a decrease in microhardness in this area down to about 434 HV0.5 (comparable with 718Plus base material) which was caused by coarsening and/or dissolution of main strengthening phases.

## 5. Conclusions

718Plus exhibits better stability of mechanical properties than the IN718 after heat treatment at 760 °C. It is caused mainly due to the thermal stability of strengthening  $\gamma'$  phase.

Microhardness of FZ after exposure at 760 °C exhibited a significant increase in hardness from 300 HV0.5 (as-welded condition) to 500 HV0.5 and approached hardness of 718Plus.

Heat treatment at 760 °C yields in the formation of complex precipitates along the interdendritic regions in the FZ. The transformation of Laves to  $\sigma$  phase occurred.

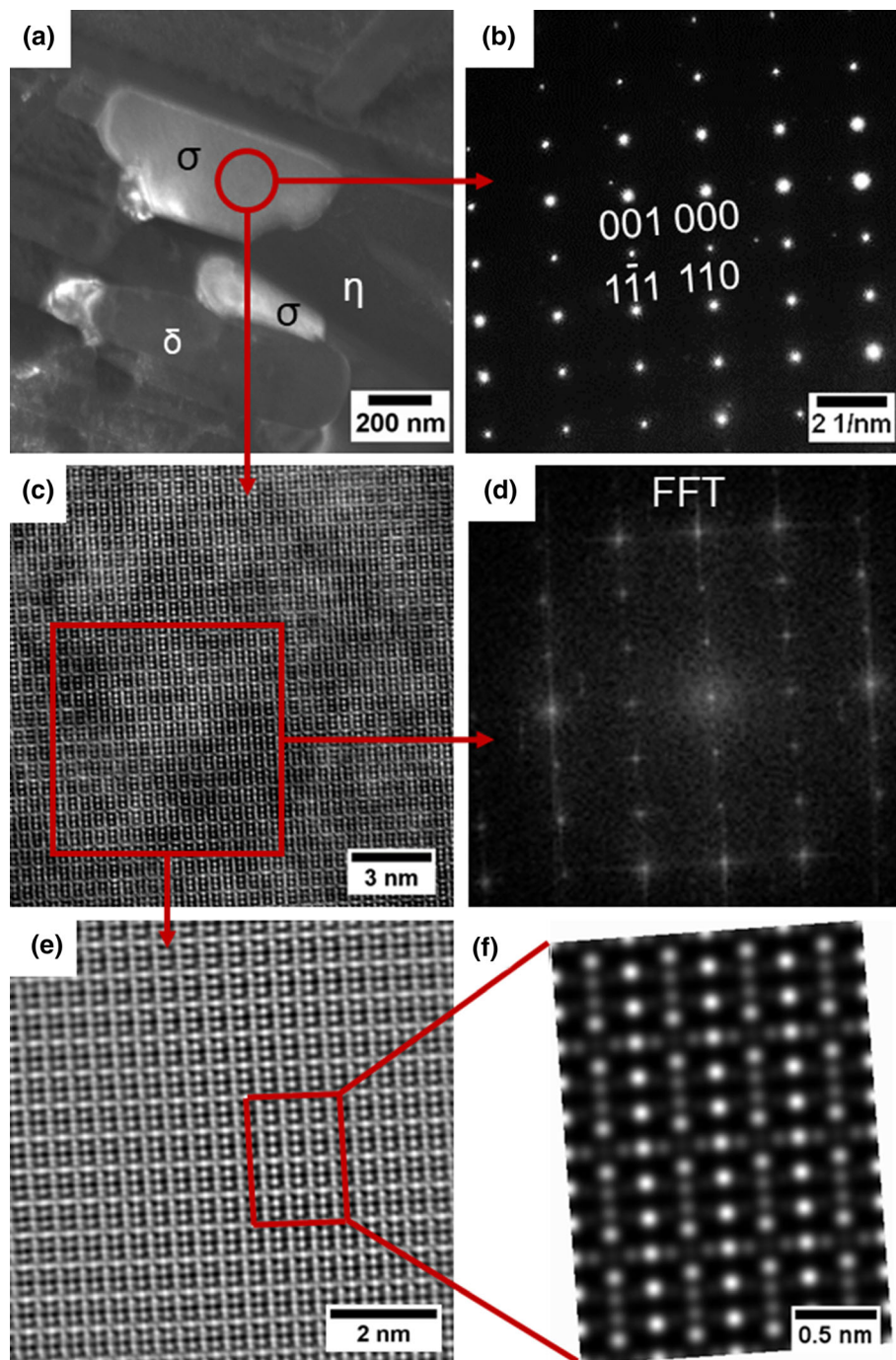


**Fig. 5** (a) TEM-DF image using (001) reflection of interdendritic region of the fusion zone with  $\sigma$  phase, (b) SAED pattern of  $\sigma$  phase ([110] ZA) taken in the area marked by circle in the TEM-DF image, (c) HRSTEM-HAADF image of  $\sigma$  phase, (d) FFT of (c), (e) filtered HRSTEM-HAADF image of  $\sigma$  phase, (f) calculated image of  $\sigma$  phase

## Acknowledgments

The authors acknowledge Pratt & Whitney, CT, for providing the material used in this investigations and for financial support under Contract No. 24117. We acknowledge partial funding from the European Union's Horizon 2020 Research and Innovation Program under Agreement No. 823717 ESTEEM3. Part of the study was performed within fundamental research financed by

AGH University of Science and Technology under project number 16.16.110.663.

## Open Access

This article is licensed under a Creative Commons Attribution 4.0 International License, which permits use, sharing, adaptation,



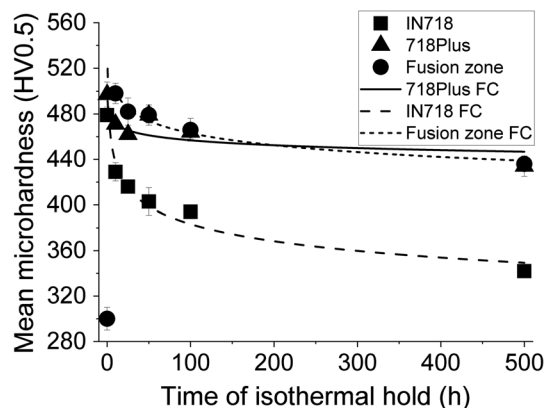


**Fig. 6** Changes of Vickers microhardness (HV0.5) with isothermal hold time of selected areas of welded joint (FC-fitting curves)

distribution and reproduction in any medium or format, as long as you give appropriate credit to the original author(s) and the source, provide a link to the Creative Commons licence, and indicate if changes were made. The images or other third party material in this article are included in the article's Creative Commons licence, unless indicated otherwise in a credit line to the material. If material is not included in the article's Creative Commons licence and your intended use is not permitted by statutory regulation or exceeds the permitted use, you will need to obtain permission directly from the copyright holder. To view a copy of this licence, visit <http://creativecommons.org/licenses/by/4.0/>.

## References

1. D.F. Paulonis and J.J. Schirra, Alloy 718 at Pratt & Whitney - Historical Perspective and Future Challenges, *Superalloys 718, 625, 706 and Various Derivatives*, E.A. Loria, Ed., TMS (The Minerals, Metals & Materials Society), Pittsburgh, 2001, p 13–23
2. H.J. Wagner, A.M. Hall, Physical Metallurgy of Alloy 718, Def. Met. Inf. Center, Battelle Meml. Inst. Columbus Ohio, 1965, Report 217, p 1–23
3. K. Kulawik, P.A. Buffat, A. Kruk, A.M. Wusatowska-Sarnek, and A. Czyrska-Filemonowicz, Imaging and Characterization of  $\gamma'$  and  $\gamma''$  Nanoparticles in Inconel 718 by EDX Elemental Mapping and FIB-SEM Tomography, *Mater. Charact.*, 2015, **100**, p 74–80
4. M. Cemal, S. Cevik, Y. Uzunonut, F. Dilemiz, ALLVAC 718 Plus™ Superalloy for Aircraft Engine Applications, *Recent Advances in Aircraft Technology*, R.K. Agarwal, Ed., 2012, p 75–96
5. R.L. Kennedy, Allvac 718Plus, Superalloy for the Next Forty Years, *Superalloys 718 625 716 and Derivatives*, E.A. Loria, Ed., TMS (The Minerals, Metals & Materials Society), Pittsburgh, 2005, p 1–14
6. J.F. Radavich, T. Carneiro, A microstructural study of alloy 718Plus™, *Superalloys 718, 625, 706 and Derivatives 2005*, E.A. Loria, Ed., TMS (The Minerals, Metals & Materials Society), 2005, p 329–340
7. K. Löhnert and F. Pyczak, Microstructure Evolution in the Nickel Base, *7th International Symposium on Superalloy 718 and Derivatives*, E.A. Ott, J.R. Groh, A. Banik, I. Dempster, T.P. Gabb, R. Helmink et al., Ed., TMS (The Minerals & Materials Society), Pittsburgh, 2010, p 877–891
8. A. Kruk, G. Cempura, S. Lech, and A. Czyrska-Filemonowicz, STEM-EDX and FIB-SEM Tomography of Allvac 718Plus Superalloy, *Arch. Metall. Mater.*, 2016, **61**, p 535–541
9. W.-D. Cao, Thermal Stability Characterization of Ni-Based ATI, 718Plus Superalloy, *Superalloys 2008*, R.C. Reed, K.A. Green, P. Caron, T.P. Gabb, M.G. Fahrman, E.S. Huron et al., Ed., TMS (The Minerals, Metals & Materials Society), Champion, 2008, p 789–797
10. J. Andersson, G. Sjöberg, J. Larsson, Investigation of Homogenization and its Influence on the Repair Welding of Cast Allvac 718Plus, *7th International Symposium on Superalloy 718 and Derivatives*, E.A. Ott, J.R. Groh, A. Banik, I. Dempster, T.P. Gabb, R. Helmink et al., Ed., TMS (The Minerals, Metals & Materials Society), Pittsburgh, 2010, p 439–449
11. M. Fisk, A. Lundbäck, J. Edberg, and J.M. Zhou, Simulation of Microstructural Evolution During Repair Welding of an IN718 Plate, *Finite Elem. Anal. Des.*, 2016, **120**, p 92–101
12. K.R. Vishwakarma, N.L. Richards, and M.C. Chaturvedi, Microstructural Analysis of Fusion and Heat Affected Zones in Electron Beam Welded ALLVAC ® 718PLUS™ Superalloy, *Mater. Sci. Eng. A*, 2008, **480**, p 517–528
13. K.R. Vishwakarma, N.L. Richards, and M.C. Chaturvedi, Haz Microfissuring in Eb Welded Allvac 718 Plus™ Alloy, *Superalloys 718, 625, 706 and Derivatives*, E.A. Loria, Ed., TMS (The Minerals, Metals & Materials Society), Pittsburgh, 2005, p 637–648
14. J. Andersson, Weldability of Precipitation Hardening Superalloys – Influence of Microstructure, Ph.D. Thesis, Chalmers University of Technology, 2011
15. M. Banasik and J. Dworak, *Poradnik inżyniera. Spawalnictwo*, WNT, Warszawa, 2005
16. A. Kruk and G. Cempura, Application of Analytical Electron Microscopy and FIB-SEM Tomographic Technique for Phase Analysis in As-Cast Allvac 718Plus Superalloy, *Int. J. Mater. Res.*, 2019, **110**, p 3–10
17. J.F. Radavich and G.E. Korth, High Temperature Degradation of Alloy 718 after Longtime Exposures, *Superalloys 1992 (Seventh International Symposium)*, S.D. Antolovich, R.W. Stusrud, R.A. MacKay, D.L. Anton, T. Khan, R.D. Kissinger et al., Ed., TMS (The Minerals, Metals & Materials Society), Warrendale, 1992, p 497–505
18. J.Y. Guédou, G. Simon, and J.M. Rongvaux, Development of Damage Tolerant Inco 718 for High Temperature Usage, *Superalloys 718, 625, 708 and Various Derivatives*, E.A. Loria, Ed., TMS (The Minerals, Metals & Materials Society), Warrendale, 1994, p 509–522
19. R. Krakow, D.N. Johnstone, A.S. Eggeman, D. Hünert, M.C. Hardy, C.M.F. Rae et al., On the Crystallography and Composition of Topologically Close-Packed Phases in ATI, 718Plus®, *Acta Mater.*, 2017, **130**, p 271–280
20. E.J. Pickering, H. Mathur, A. Bhowmik, O.M.D.M. Messé, J.S. Barnard, M.C. Hardy et al., Grain-Boundary Precipitation in Allvac 718Plus, *Acta Mater.*, 2012, **60**, p 2757–2769

**Publisher's Note** Springer Nature remains neutral with regard to jurisdictional claims in published maps and institutional affiliations.